ICAS-80-4.2 ENGINE AIR INTAKE DESIGN SUPPORT BY USE OF COMPUTATIONAL METHODS AND COMPARISON OF THEORETICALLY DERIVED PRESSURE DISTRIBUTIONS WITH EXPERIMENTAL DATA

A. Eberle and D. M. Schmitz
Aerodynamic Department
Messerschmitt-Bölkow-Blohm GmbH
Postfach 801160
8000 München 80
West-Germany

Abstract

Within the frame of flow simulation past intakes by numerical methods computer codes were developed for the solution of the full potential equation by finite elements and EULER's equations by an implicit finite difference scheme. The following items proved to be important for obtaining acceptable results.

- conservative artificial density scheme for the potential variational principle
- semi orthogonal grid generation
- characteristic boundary algorithm for EULER's equations.

Comparisons with elaborate experiments prove engineering usefulness of the proposed approach.

Experimental Investigation

During the development of the TORNADO fighter aircraft a 1:6.5 intake model was tested in the 8 x 8 ft transonic wind tunnel at ARA Bedford (fig. 1).

These tests included the measurement of pressure distributions on the ramps and on the external and internal cowl lip.

Fig. 2 shows the general arrangement of the 2-dimensional, double wedge intake.

The first wedge angle was 7 degrees, the moveable ramps were in the fully open position for the data shown in this paper. The AAID's were closed. The mass flow through the intake model was controlled by a variable position plug at the duct exit. The mass flow was measured by an internal venturi nozzle.

The instrumentation for the data being used for the comparison with theoretically derived data consisted of 14 static pressure orifices on the ramps of the port intake (5 on the 1st, 5 on the 2nd, and 4 on the 3rd ramp), and of 16 static pressure orifices on the cowl lip of the starboard intake, of which 5 were located on the lower surface (external) and 11 on the upper surface (internal) (fig. 3).

The Mach number varied from 0.7 to 1.3, and the test angles of attack were 0 and 3 degrees.

For all test points, the Reynolds number range was from 1.24 to 1.45 million per meter.

Numerical Approach

Scope of Computational Procedures

The present study investigates choice and development of computer programs being able to evaluate the pressure distribution along the intake walls. For this purpose the flow model is drastically simplified by assuming two-dimensional inviscid flow in a mean surface cutting vertically through the box-type intake. At some distance downstream of the intake lips the geometry is thought to be extended to infinity by straight parallel lines.

Two classes of approach are possible

- potential theory
- EULER's equations

Numerous codes were developed solving the full potential equation in the transonic range [1÷3] and successful flow simulations past intakes could be performed some of which are listed in this paper. However, if the freestream Mach number exceeds unity this approach is no more adequate due to large stagnation pressure losses at shocks which are not accounted for by the defining equations of isentropic flow. A solution to this problem is offered, by the integration of EULER's equations, which is, however, no more a trivial task. Since we did not succeed after having reprogrammed approximately 15 versions well documented in literature we tried to find an own reliable solver for EULER's equations.

Investigations Based on Full Potential Equation (FPE)

a. Basic Equations

Since numerous codes using a variatio-

nal principle finite element formulation proved successful for transonic flow computations it was attempted to use the same method for intake calculations. The governing equation is easily derived for an irrotational fluid from BERNOULLI's equation written in a streamline aligned coordinate system

$$p_s + \varrho q q_s = 0$$

Using the chain rule of differentiation this equation can be transformed into

$$p_\phi + \varrho q q_\phi = 0$$

with

$$q = \sqrt{\phi_x^2 + \phi_z^2}$$

Partial integration gives

$$\iint (p_\phi + \varrho q q_\phi)\, dxdz =$$

$$= \iint [p_\phi - \phi_\phi \mathrm{div}(\varrho \vec{q})]\, dxdz + \oint \varrho \phi_\phi \phi_n ds = 0$$

The second term of the area integral vanishes due to mass conservation inside the flow field. At solid boundaries the surface integral becomes zero because of $\phi_n = 0$ and at farfield boundaries because the total mass flux cancels. So our govering equation assumes the simple form

$$\iint p_\phi dxdz = \iint \varrho q q_\phi dxdz = 0$$

b. Rotated Upwinding Scheme [9]

Equation a. provides no mean for stabilizing a numerical procedure if the local Mach number exceeds unity. Since streamwise density upwinding often used in finite element methods fails at high free stream velocity and/or angles of attack the following new fully conservative artificial density scheme was developed which depends on the orientation of the computational cell with respect to the associated pivotal point.

The artificial density in a cell A adjacent to controlpoint P is evaluated by the following expression (see sketch).

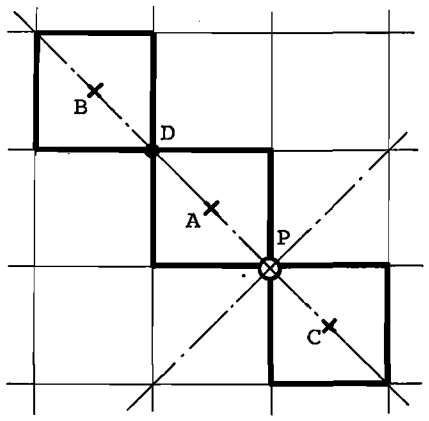

$$\varrho = \varrho_A + \frac{1}{4}\left[(\mu_A+\mu_B)\,\Delta_{BA}(1+\alpha) + (\mu_A+\mu_C)\Delta\varrho_{CA}(1-\alpha)\right]$$

with

$$\alpha = \frac{\Delta\phi_{PD}}{|\Delta\phi_{PD}|},\quad \mu = \max\left(0, 1 - \frac{1}{M^2}\right)$$

The potential derivative of a. is replaced by $\partial/\partial\phi_i$, i = 1 ... N, where the i's count the nodal values of our computational grid. After replacing the potential distribution in between the gridlines by bilinear isoparametric elements the integration can be performed numerically using GAUSS' 4-point rule. The resulting system of quasi linear equations is solved by successive line overrelaxation.

FPE-Results

Figures 4 and 5 are results of the proposed finite element method. The grids were obtained by solving two LAPLACE-equations for x and z. The example of fig. 4 shows a nicely developed supersonic bubble above the upper lip which is terminated by a strong shock. No overshoot in front of the steep pressure gradient is observed. The second calculation was performed for a slightly supersonic freestream. The dots indicate supersonic cells. Mach numbers higher than the present caused divergence of the code.

Investigations Based on the Solution of EULER's Equations

a. Basic Equations

The following procedure is based on these equations written in quasilinear form for the variables ϱ, $m = \varrho u$, $n = \varrho w$

$$\begin{pmatrix} \dot{\varrho} \\ \dot{m} \\ \dot{n} \end{pmatrix} + A \begin{pmatrix} \varrho_x \\ m_x \\ n_x \end{pmatrix} + B \begin{pmatrix} \varrho_z \\ m_z \\ n_z \end{pmatrix} = 0$$

where A and B are matrices containing members which are functions of the velocity components. Since we are only interested in steady state solutions the pressure is replaced by the constant total enthalpy equation

$$p = \varrho\left(1 - \frac{\varkappa-1}{2\varkappa} q^2\right)$$

b. Boundary Algorithm

Provided system a. should be solved by a finite difference scheme it is clear that at all computational boundaries one sided differences would occur.

Such a procedure is either unstable and/

or enters an unacceptable large error exactly at those points where high accuracy is required. So we replaced all derivatives *normal* to the boundaries by characteristic compatibility equations generating an algorithm which transports perturbation energy without reflection out of the computational flow field.

For this purpose the governing equations a. are locally transformed in a cartesian coordinate system aligned with the boundary under consideration such that the x-axis is tangent and the z-axis is normal to it.

Now system a. is extended by the linear TAYLOR expansion of the variables along a characteristic vector pointing from the present time level back to the previous with components 0, Δz, $-\Delta t$

$$\begin{pmatrix} g \\ m \\ n \end{pmatrix}^{-} = \begin{pmatrix} g \\ m \\ n \end{pmatrix} - \begin{pmatrix} g \\ m \\ n \end{pmatrix}^{\bullet} \Delta t + \begin{pmatrix} g \\ m \\ n \end{pmatrix}_z \Delta z$$

leading to

$$\begin{pmatrix} g' \\ m' \\ n' \end{pmatrix} + A \begin{pmatrix} g_x \\ m_x \\ n_x \end{pmatrix} + (B + \dot{z}) \begin{pmatrix} g_z \\ m_z \\ n_z \end{pmatrix} = 0$$

Since each component of this vector equation is zero the inner product with another vector composed of three arbitrary components (a, b, c) also vanishes and gives a scalar equation of the form

$$ag'+bm'+cn'+\bar{a}g_z+\bar{b}m_z+\bar{c}n_z = \bar{r}$$

where $\bar{a}$, $\bar{b}$, $\bar{c}$ can be made vanish for suitable choices of $\dot{z}$. Finally two of the components of the eigenvector (a, b, c) can be expressed as functions of the remaining component and the eigenvalues $\dot{z}_{1,2,3}$. After these lengthy operations the normal characteristic compatibility equation is obtained:

$$Rg+Mm+Nn = f(g^{-},m^{-},n^{-},g_x,m_x,n_x)$$

The coefficients R, M, N and the tangential derivatives have to be evaluated at the newest time level which requires at least two iterates. Base point interpolation of g^{-}, m^{-}, n^{-} is achieved by a TAYLOR series expansion around grid points closest to the latter.

c. Boundary Value Count

From the considerations of b. it can be found that as many boundary values have to be prescribed as eigenvelocities $\dot{z}$ point outward of the computational domain. The result is summarized in fig. 6.

d. Interior Point Algorithm

After all quantities have been computed along the boundaries for the time level under consideration we are ready to update the interior points using a simple semi implicit line relaxation scheme along the ζ-lines of the mesh which requires only two iterates, see fig. 7.

Since the finite difference form is written in grid coordinates the transformation from global to local coordinates is computed numerically by the following formulae.

$$\begin{aligned} \xi_x &= z_\zeta/D \\ \xi_z &= -x_\zeta/D \\ \zeta_x &= -z_\xi/D \\ \zeta_z &= x_\xi/D \\ D &= x_\xi z_\zeta - x_\zeta z_\xi \end{aligned}$$

For faster convergence the largest local allowable time step is used, fig. 8.

e. Grid Generation

It seems to be inevitable for an accurate EULER code to generate a grid which is orthogonal at boundaries. For this purpose the rectangular grid of an auxiliary computational domain of simple geometry is mapped into the physical plane by solving two POISSON--equations for each coordinate, fig. 9.

The forcing terms on the right hand side are evaluated at the boundaries directly from these equations using imaginary points outside the grid such that the first interior row of points lies on lines cutting the boundary orthogonal. Inside the grid the source distribution is represented by linear interpolation between the boundary values. A nice by-pass result is the very fast convergence of the point GAUSS-SEIDEL procedure due to the forcing terms acting as correction to the previous iterate.

Comparison of Theory and Experiment (EULER's Equations)

Fig. 10 through 13 are the results of the present investigation. For all Mach numbers time stepping was stopped after 50 iterates since no visible change of the pressure distribution was observed when using 100 or more time surfaces. This relatively short overall time was not sufficient, however, for shifting the bow shock occuring at supersonic freestream into its final position. Nevertheless the pressure distribution seemed to be practically frozen for these cases, no matter whether the initial shock location was assumed to be way upstream of the upper pointed lip or very close to it. The dots in fig. 12 and 13 are supersonic grid points and represent a transient state of the flowfield

at M = 1.3 and a captured area ratio of 0.836 and 0.665. Since the horizontal mass flux component at the upper nose is set equal zero the front shock can be very close to it but never is attached.

Although no artificial viscosity was used the pressure distributions exhibit almost perfect smoothness. No instability was observed when a test case with 200 iterates was run. The computer time required for 50 iterates was 3 min.CPU on a IBM 3033 without bow shock algorithm and 4 min.with grid adaption to the bow shock formation. Fig. 14 through 17 compare computed results with experimental data.

All measurements are obviously affected by viscous interaction since in no case the theoretical inviscid down stream pressure is reached. At subsonic speeds the internal cowl portion exhibits steep positive inviscid pressure gradients immediately aft of the nose.

So deviation from experiment may be interpreted as local flow separation whereas the upper ramp is in good agreement (fig. 14, 15). At M = 1.3, mass flux ratio Q = 0.836 (figure 16), no comparison is made with internal data, since measurements indicated supersonic speed all along the first ramp, an effect which only may occur if the oblique front shock is attached to the nose. Due to the low number of time steps the present procedure did not detect supersonic speeds inside the intake. In the last example (fig. 17) the internal cowl portion is in good agreement, but the first ramp exhibits shock-boundary layer interaction. The external cowl distribution shows separation at the nose because of the strong flow deflection, $\alpha_{local} \approx -30°$, see also velocity vectors of fig. 13.

Conclusion

Two methods based on potential theory and EULER's equations are proposed for inviscid intake flow simulation which seem to be a useful tool for design considerations. The elements of the computer programs are designed such that they can be extended to

- threedimensional flow
- viscid interaction

The latter approach rejects not the principles of the proposed boundary algorithm, if viscous terms are treated as explicit perturbations to the inviscid equations.

References

[1] EBERLE A.
Transonic Potential Flow Computations by Finite Elements: Airfoil and Wing Analysis, Airfoil Optimization
MBB UFE1428(Ö)/DGLR 78-65 1979

[2] EBERLE A.
Transonic Flow Computation by Finite Elements: Airfoil Optimization and Analysis.
Recent Developments in Theoretical and Experimental Fluid Mechanics
Springer-Verlag Berlin Heidelberg 1979

[3] EBERLE A.
Evaluation of a Minimum Principle for Transonic Flow Computations by Finite Elements
3rd GAMM-Conference on Numerical Methods in Fluid Mechanics
Friedr.Vieweg & Sohn
Braunschweig/Wiesbaden 1979

[4] YOSHIHARA H. / MAGNUS R.
Inviscid Transonic Flow over Airfoils
AIAA paper 70-47 1970

[5] KNIGHT D.D.
Calculation of High-Speed Inlet Flows Using the NAVIER-STOKES Equations
AIAA paper 80-1107 1980

[6] BEAM R.M. / WARMING R.F.
An Implicit Factored Scheme for the Compressible NAVIER-STOKES Equations
AIAA paper 77-645 1977

[7] McCORMACK R.
A Rapid Solver for Hyperbolic Systems of Equations
Lecture Notes in Physics, Vol.59
Springer-Verlag, Berlin 1976

[8] LOTTER K.W. / BISSINGER N.C.
Dynamic Pressure Loads in the Intake of Tornado Aircraft
AGARD paper 21
52nd Meeting on Stresses, Vibration, Structural Integration and Engine Integrity 1978

[9] FORNASIER L.
A Rotated Artificial Density FEM
Aeritalia-MBB Collaboration 1980

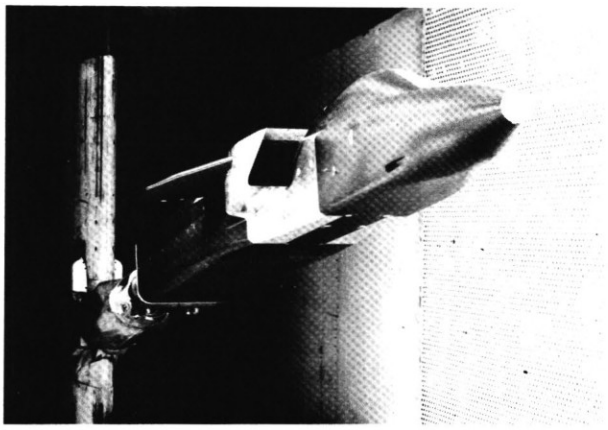

Fig. 1

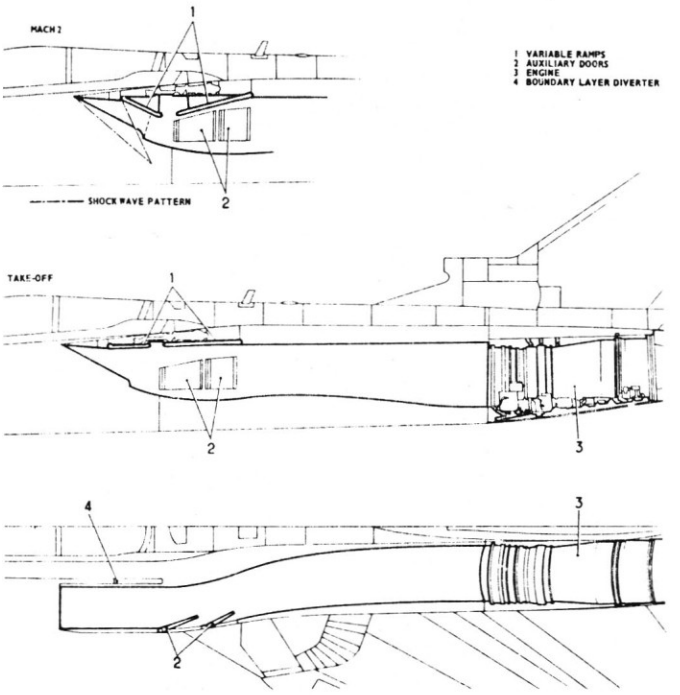

Fig. 2

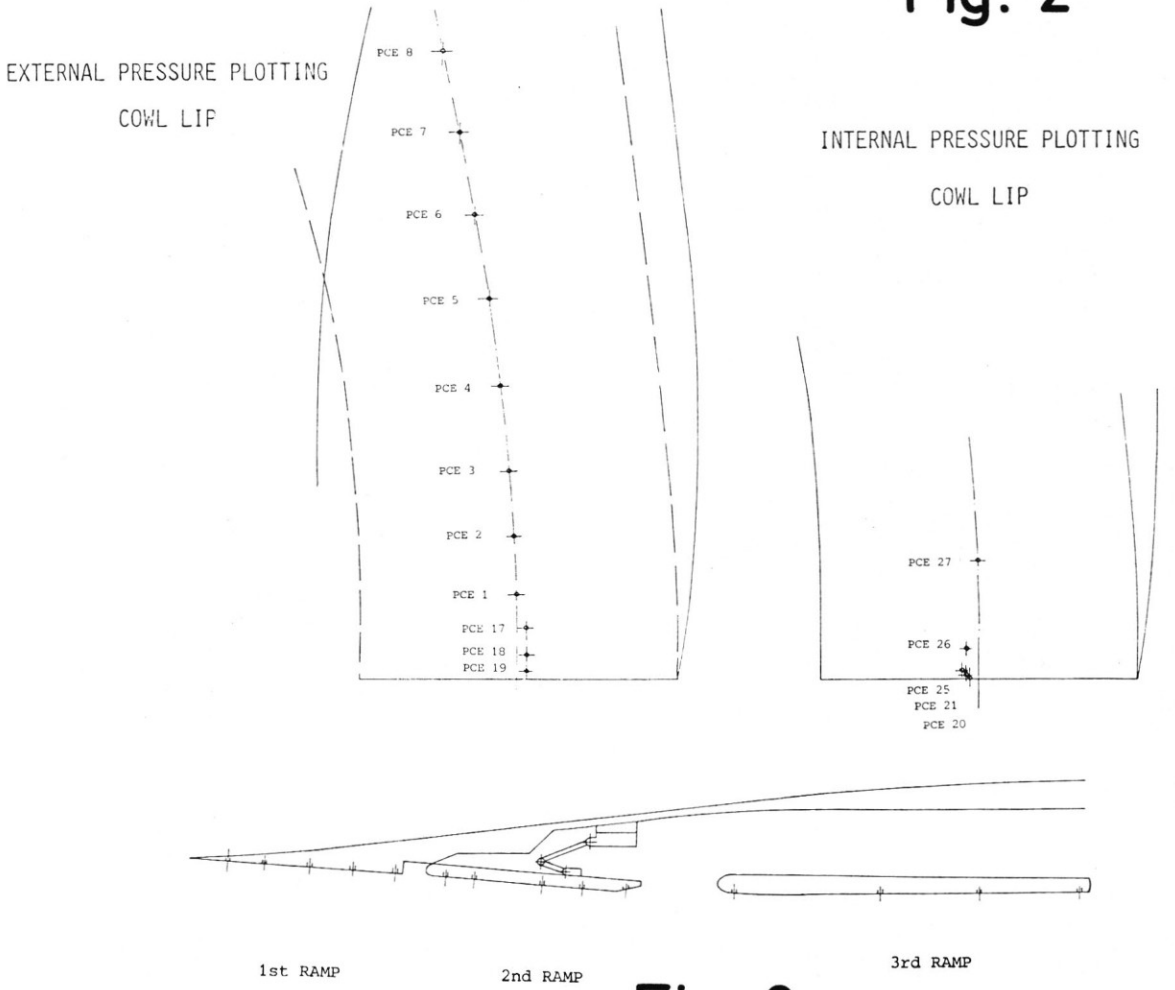

Fig. 3

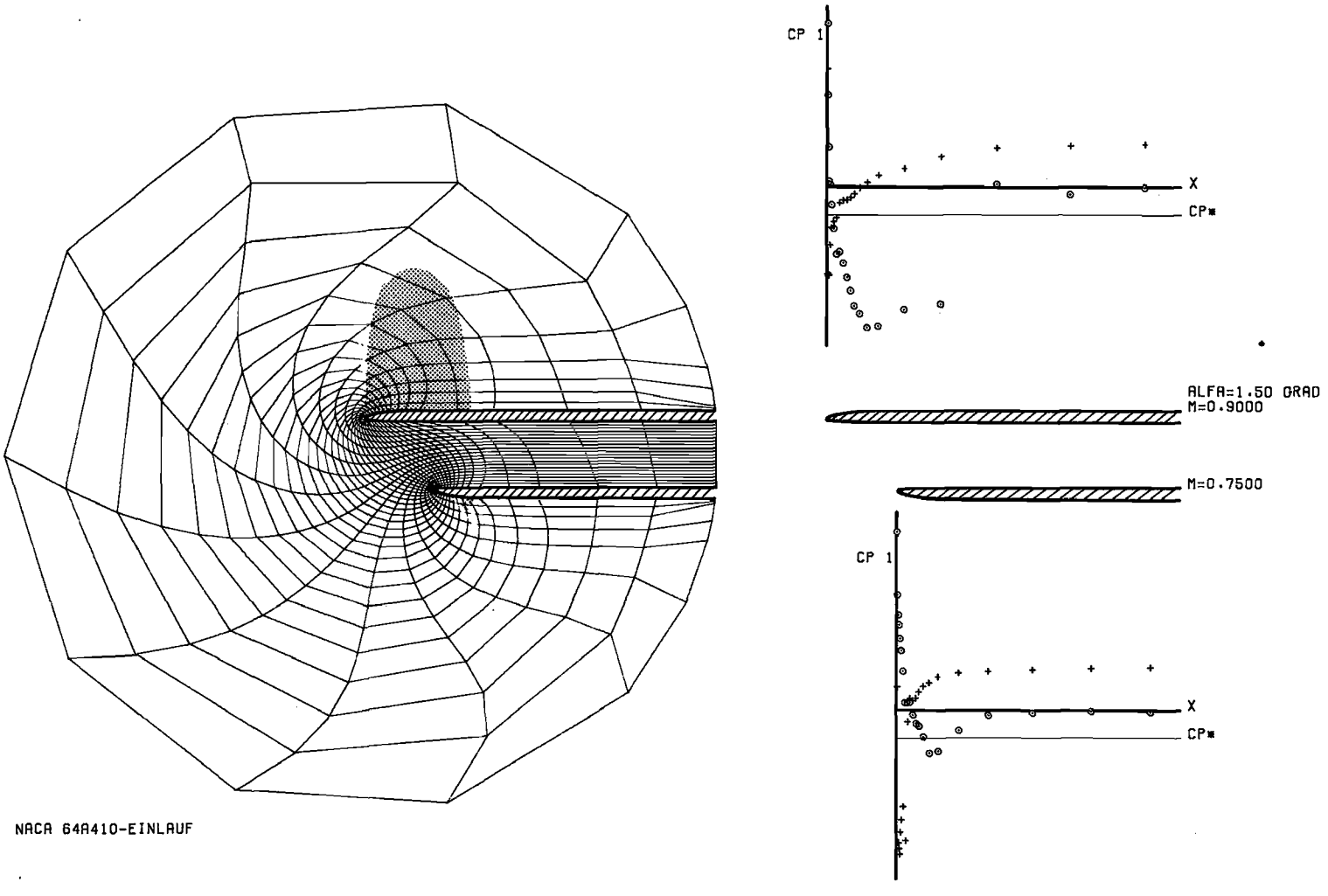

Fig. 4

ANALYSIS OF AIR-INTAKE BY FINITE ELEMENT TECHNIQUE (FPE)

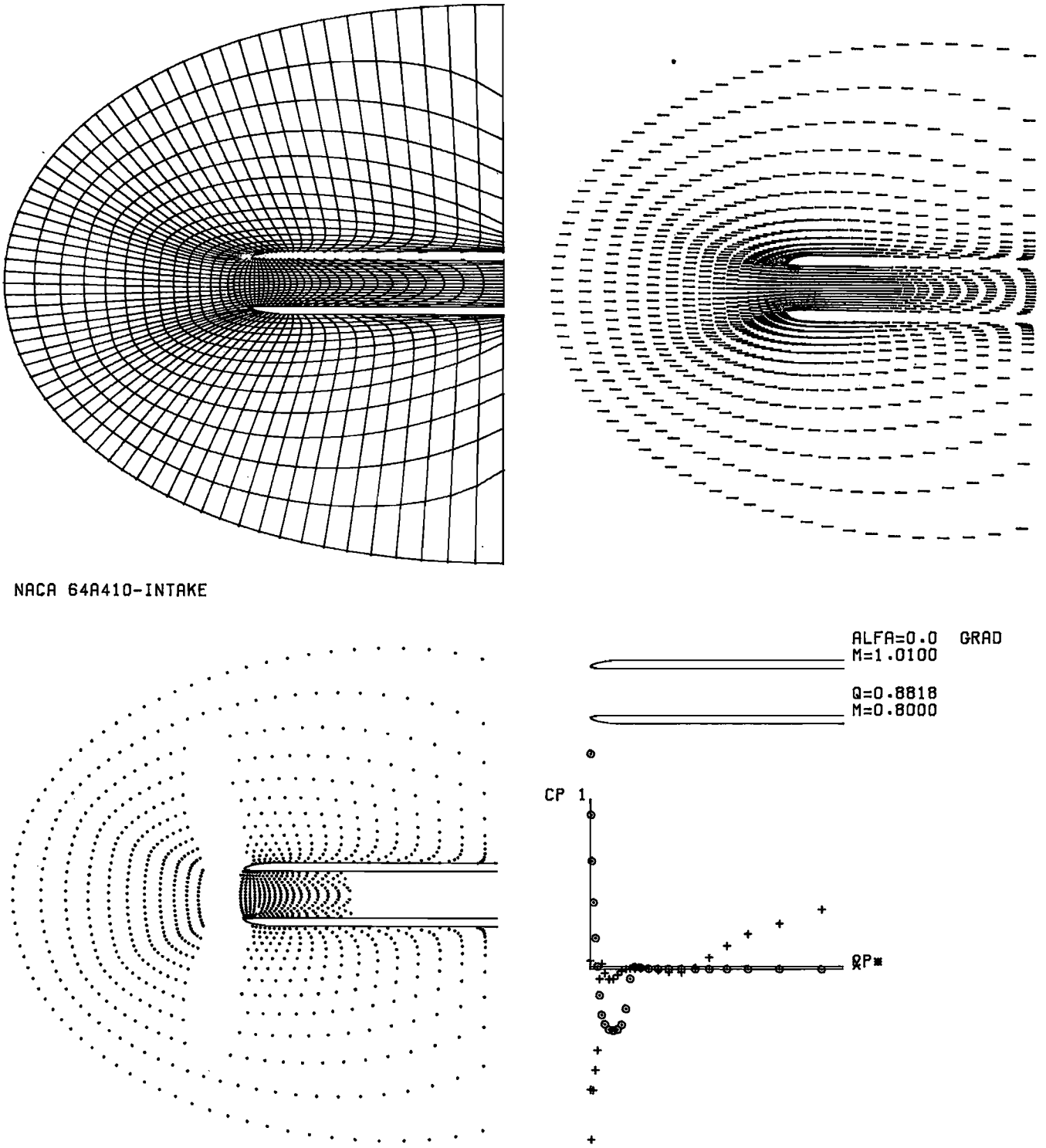

Fig. 5

Boundary Value Count

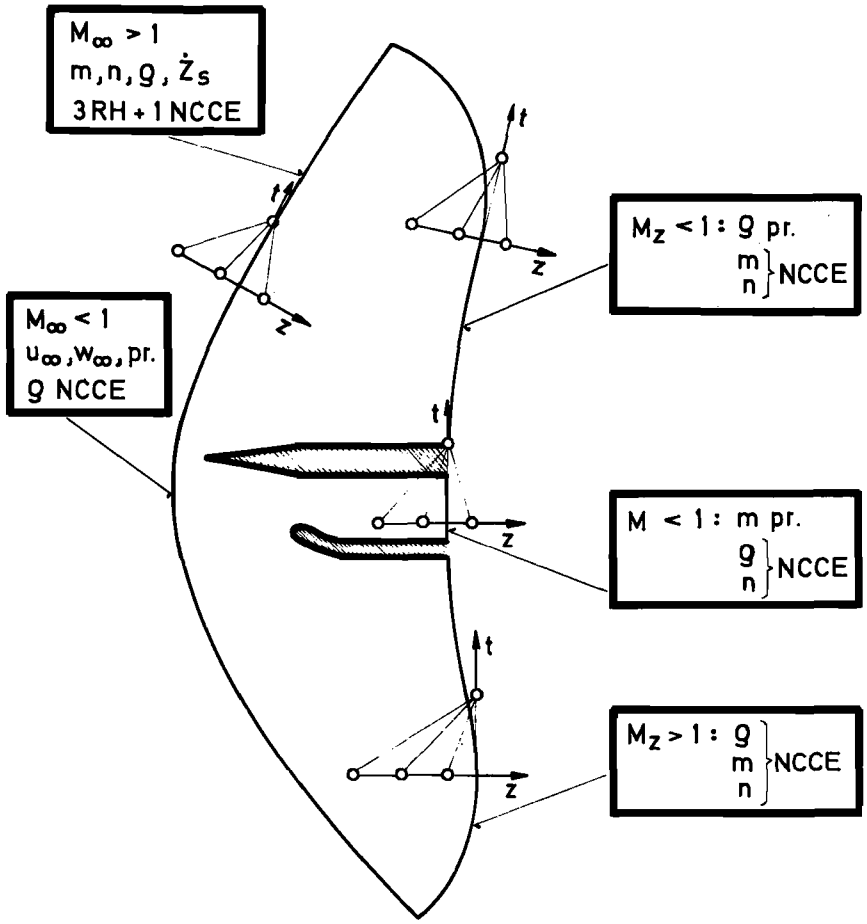

Fig. 6

RH = RANKINE-HUGONIOT
NCCE = normal characteristic compatibility eq.
pr. = prescribed

Interior Point Calculation
(backward EULER)

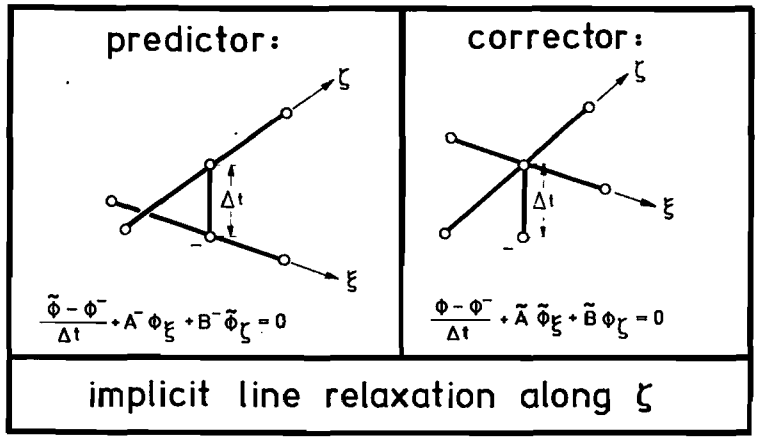

Fig. 7

Local Variable Time Step

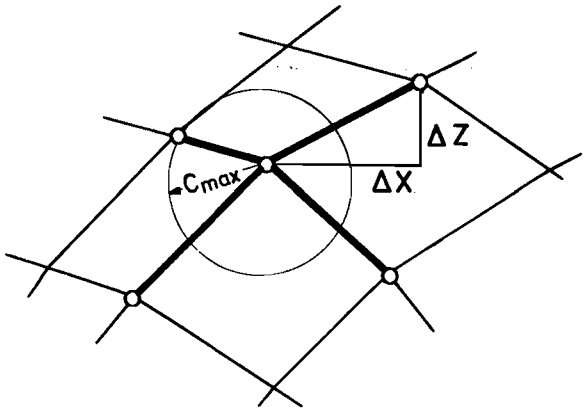

$$\Delta t = \frac{\sqrt{\min(\Delta X^2+\Delta Z^2)}}{q\,\frac{\varkappa+1}{2\varkappa}+\sqrt{1-\frac{(\varkappa+1)(\varkappa-1)}{4\varkappa^2}\,q^2}} = f(X,Z)$$

Fig. 8

Grid Generation

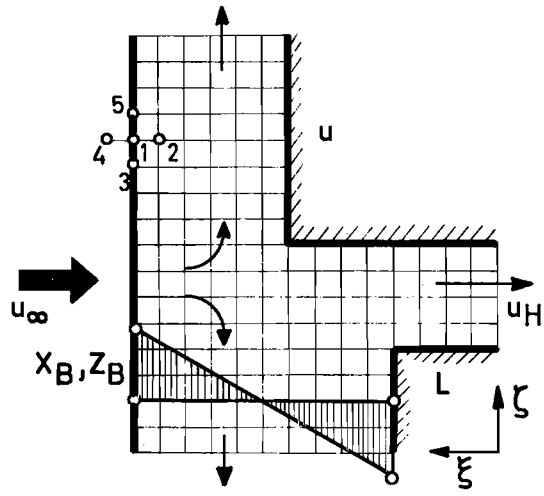

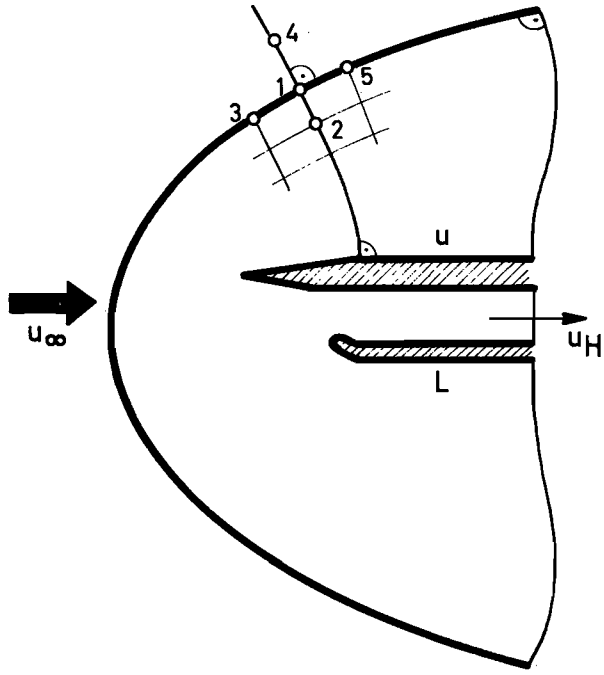

$$x_{\xi\xi} + x_{\zeta\zeta} = X$$
$$z_{\xi\xi} + z_{\zeta\zeta} = Z$$

Fig. 9

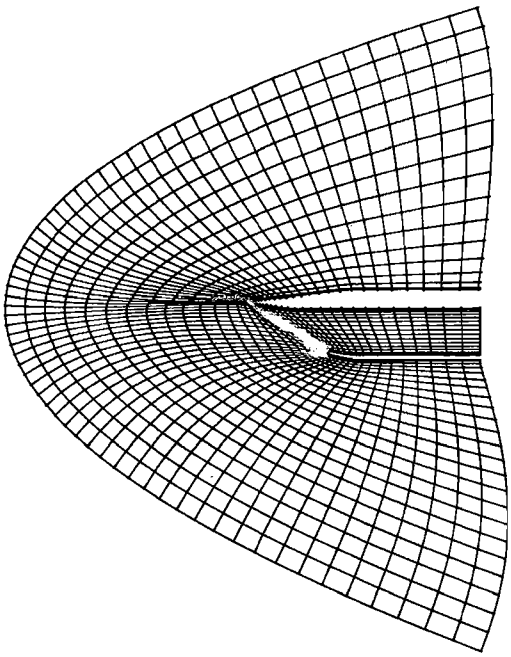

TORNADO-EINLAUF

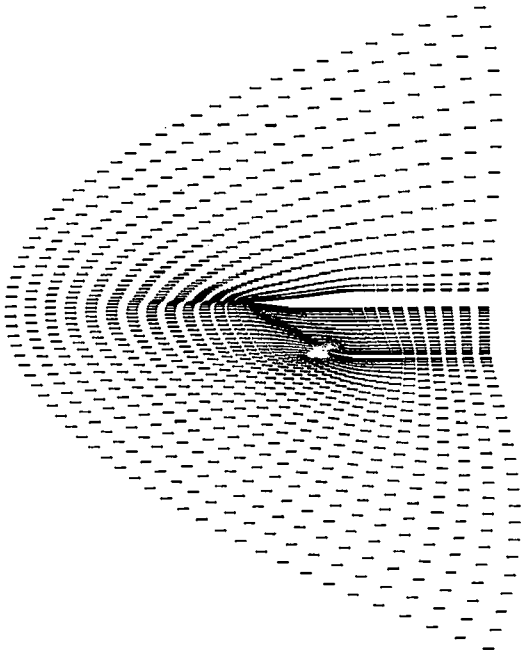

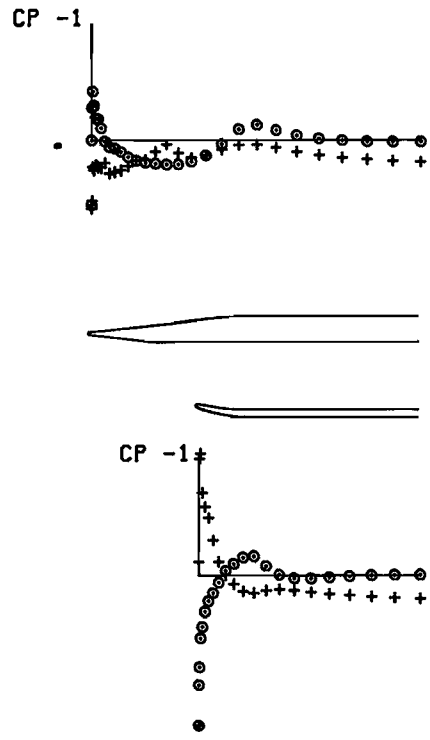

Fig. 10

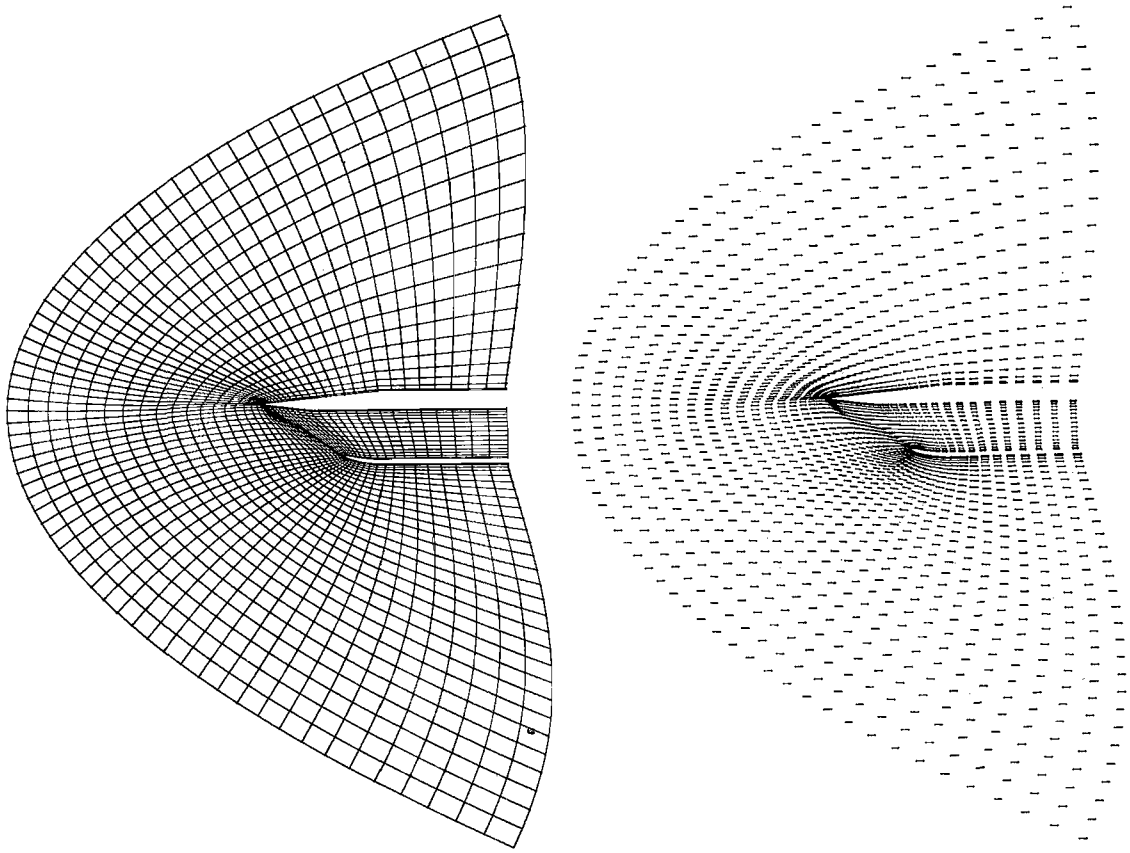

TORNADO-EINLAUF

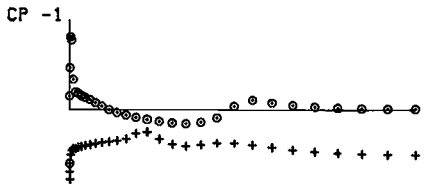

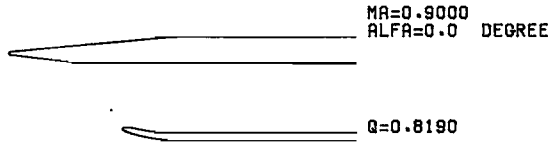

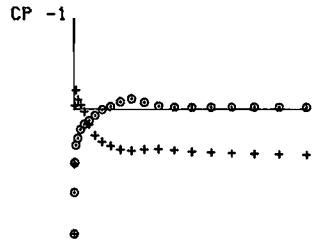

Fig. 11

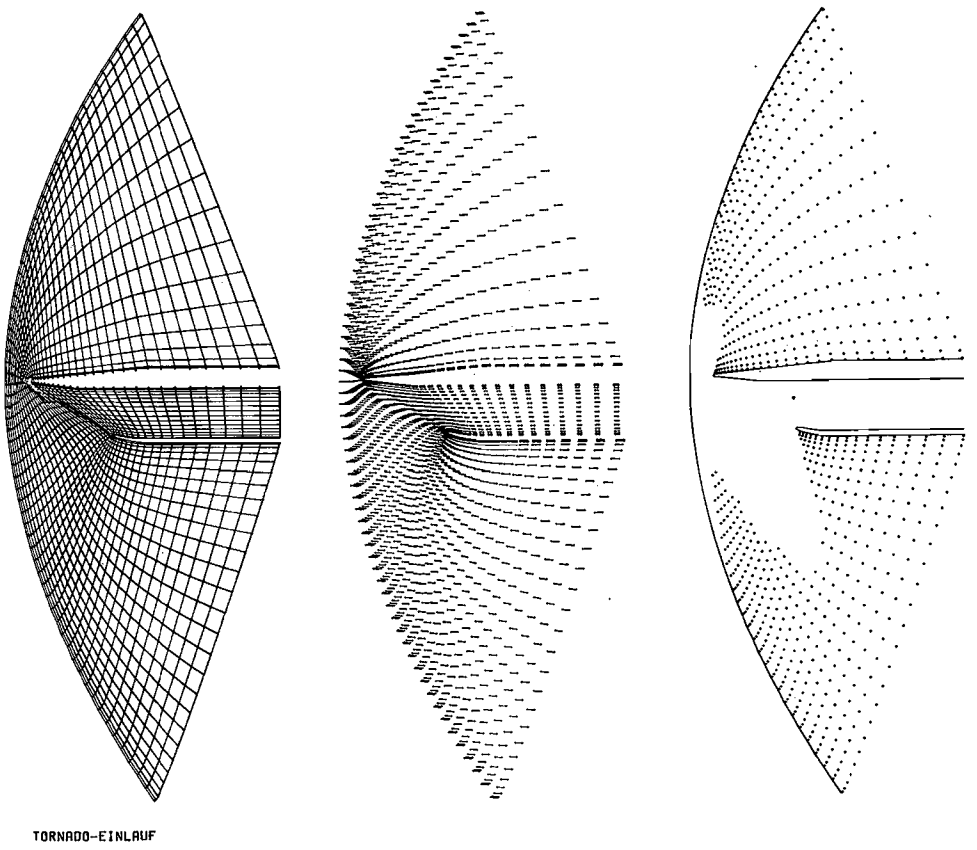

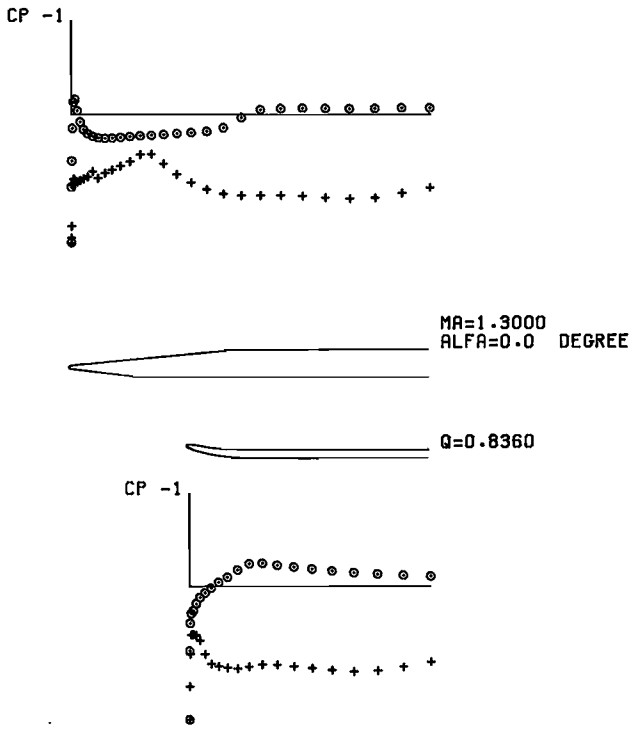

Fig. 12

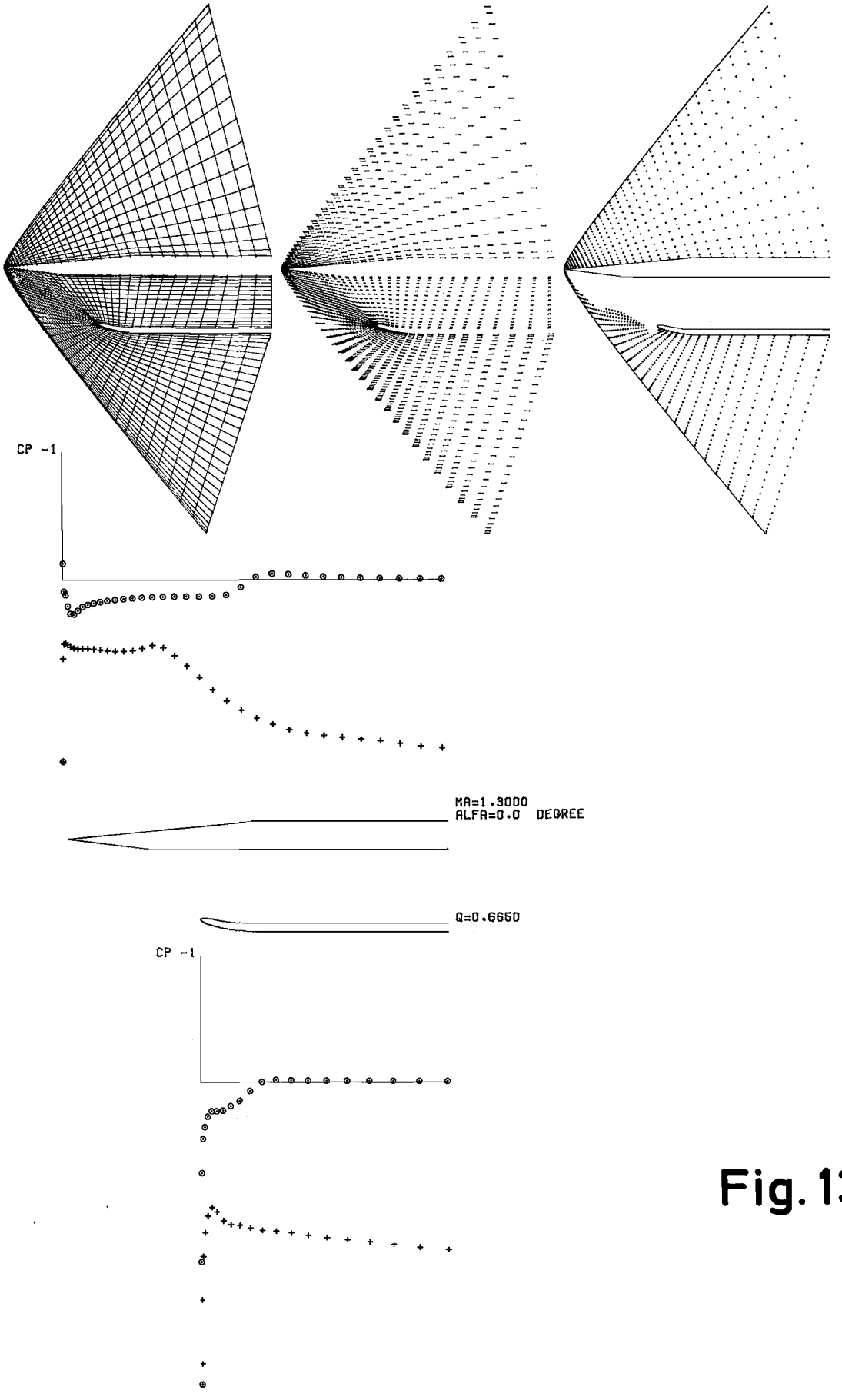

Fig. 13

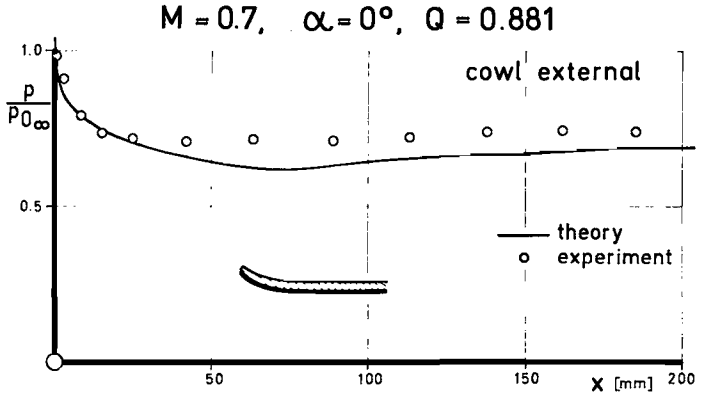
M = 0.7, α = 0°, Q = 0.881
cowl external
theory
experiment
1.0
0.5
p/p0∞
50
100
150
200
X [mm]

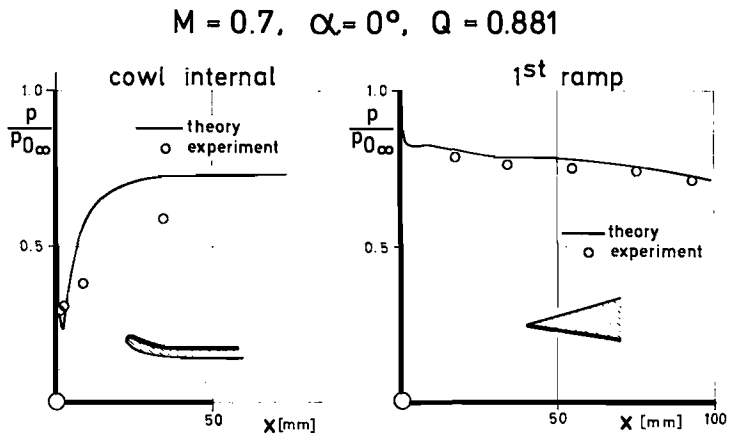
M = 0.7, α = 0°, Q = 0.881
cowl internal
1st ramp
theory
experiment
1.0
0.5
p/p0∞
50
100
X [mm]

Fig. 14

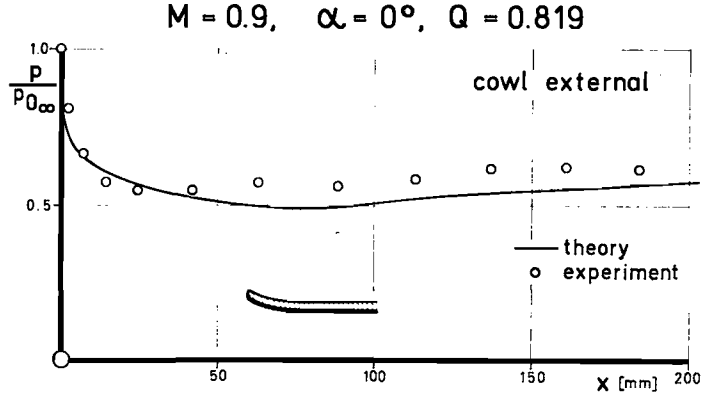
M = 0.9, α = 0°, Q = 0.819
cowl external
theory
experiment
1.0
0.5
p/p0∞
50
100
150
200
X [mm]

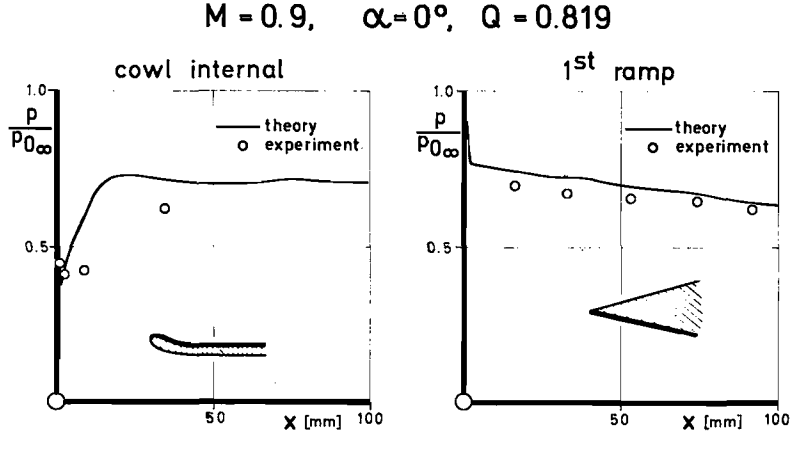
M = 0.9, α = 0°, Q = 0.819
cowl internal
1st ramp
theory
experiment
1.0
0.5
p/p0∞
50
100
X [mm]

Fig. 15

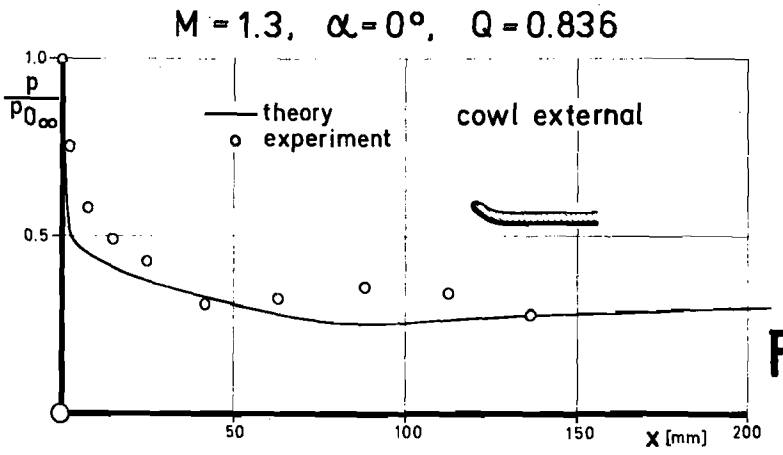
M = 1.3, α = 0°, Q = 0.836
1.0
p/p0∞
0.5
theory
experiment
cowl external
50
100
150
X [mm]
200

Fig. 16

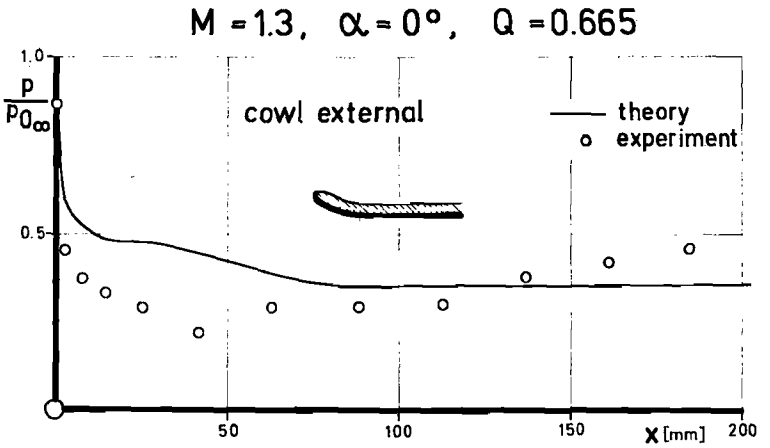
M = 1.3, α = 0°, Q = 0.665
1.0
p/p0∞
0.5
cowl external
theory
experiment
50
100
150
X [mm]
200

Fig. 17

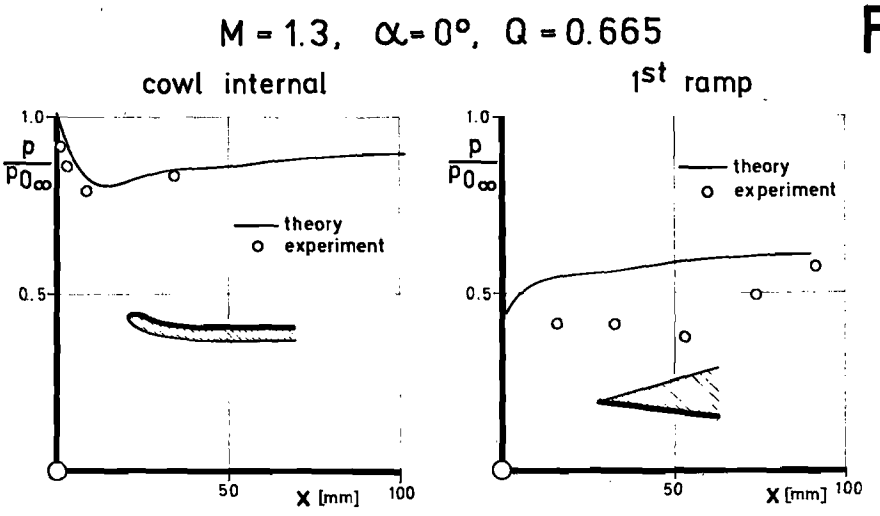
M = 1.3, α = 0°, Q = 0.665
cowl internal
1st ramp
1.0
p/p0∞
0.5
theory
experiment
50
X [mm]
100